CHARACTERIZATION OF THE UNSTEADY LEAKAGE FLOW IN AN AXIAL FAN

M. Dellacasagrande, E. Canepa, A. Cattanei, M. Moradi

DIME, University of Genova, Genova 16145, Italy

ABSTRACT

The present work reports an experimental study of the leakage flow in a low-speed ring fan. Existing 2D Particle Image Velocimetry (PIV) measurements taken in a meridional plane in front of the rotor gap have been further processed and analyzed by means of the Proper Orthogonal Decomposition (POD). Three values of the dimensionless pressure rise across the rotor have been investigated. Namely, attention has been focused on the intermediate case, the one for which a strong radial oscillation in the leakage flow has been observed: the POD has shown that, at this condition, the leakage flow has a periodic character that is not correlated to the periodic blade passing. Moreover, such coherent motions have been found to promote turbulence transport at different radial positions, a behavior that was not observed for the periodic fluctuations related to the rotor. The present POD procedure can be therefore generally applied to turbomachinery flows to characterize their unsteady behavior beside the classical phase-averaging methods based on rotor related quantities. The present approach is novel for the leakage flow study.

KEYWORDS

axial-flow fan, rotating shroud, leakage flow, PIV, POD

NOMENCLATURE

u	fluctuating axial velocity	Ω	rotational speed
v	fluctuating radial velocity	Q	volume flow rate
$\overline{u}$	time-mean axial velocity	Φ	flow coefficient
$\overline{v}$	time-mean radial velocity	Δp	pressure rise across the rotor
Ψ	loading coefficient	**Subscripts**	
θ	phase angle	ROT	rotor related quantity
TKE	turbulent kinetic energy	POD	POD related quantity
P_{TKE}	turbulent kinetic energy production		

INTRODUCTION

Axial fans employed in automotive cooling systems are commonly provided with a rotating shroud, a ring connecting the blade tips that improves the volumetric efficiency and also strengthens the whole assembly. Unfortunately, it causes a strong increase in the radiated noise due to the presence of coherent flow structures (Longhouse 1978) that are contained in the leakage flow released from the gap between the ring and the stationary enclosure, and are eventually re-ingested by the rotor. Such a noise is often predominant in the low- to medium-frequency range and may also constitute the major contribution to the radiated power, e.g. see Canepa et al (2016, 2019a). The qualitative features of the leakage flow are known, e.g. see Fukano et al (1986), Fukano and Jang (2004), Piellard et al (2014), Magne et al (2015), Moreau and
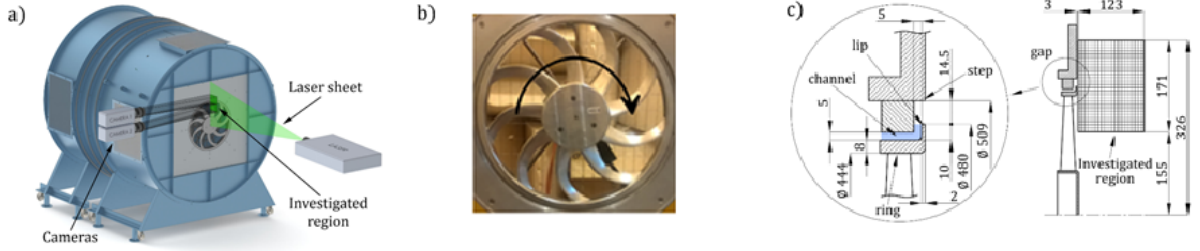
Figure 1: Experimental facility: (a) test rig; (b) rotor prototype; (c) rotor geometry.

Sanjose (2016), Zenger et al (2016), Na et al (2017), Canepa et al (2018, 2019b, 2021), and Zhu et al (2018). However, coherent flow structures generally constitute a rather complicated fluid dynamic problem and, in the present case, their properties are not completely known: the fact that noise humps at sub-harmonics of the blade passing frequency appear indicates that they are co-rotating, but the relation with gap geometry and operating point is not completely clear. In order to find effective solutions for noise reduction and also to provide reliable test cases for numerical simulations, a deeper insight in these aspects is necessary.

The present paper continues the aerodynamic investigation reported in Canepa et al (2021), which was based on 2D PIV measurements taken in the meridional plane. In such a study, a detailed analysis of the effect of the operating point on the leakage flow pattern was reported. Namely, it was showed that, about the design operating point, a sudden modification in the flow pattern takes place that strongly affects the radiated noise. Such a modification consists in a switch between a recirculating flow attached to the ring lip directly re-ingested by the rotor, and a radial flow that mixes with the main rotor inflow. By means of conditional averages, it was also shown that, when the modification takes place, both flow patterns are present together with all of the intermediate ones. However, it was not possible to deepen the features of the transition and also whether such patterns follow a regular time sequence or they alternate randomly. In the present paper, the coherent flow structures embedded in the flow are studied by means of a POD-based procedure employing a phase averaging technique previously presented in Lengani et al (2014). This approach has allowed us to separate the periodic part of the flow related to the rotor revolution from the one related to the leakage flow fluctuation that is not correlated to the rotor position.

EXPERIMENTAL SETUP AND MEASURING TECHNIQUES

Data presented here are a part of the experimental data base collected in the previous authors' work Canepa et al (2021). The measurement campaign has been carried out in the DIME Aeroacoustics laboratory with the fan mounted on a test rig designed based on ISO 5801 norms, see Fig. 1a. The tested rotor is a 9-blade aluminum prototype obtained by means of a numerically controlled milling machine (Fig. 1b). The rotor stiffness prevents the geometry from being altered by aerodynamic load and centrifugal force, avoiding cross-effects on the modification of the leakage flow, e.g., see Canepa et al (2018). The rotor has a tip radius r_{tip} of 222 mm, a hub-to-tip radius ratio r_{hub}/r_{tip} of 0.374, and a chord that varies between 43 mm and 50 mm from hub to tip. At the design point, the flow coefficient is $\Phi_{des} = Q_{des}/(u_{tip}\pi r_{tip}^2) = 0.0869$, and the pressure rise coefficient is $\Psi_{des} = \Delta p_{des}/(0.5\rho_0 u_{tip}^2) = 0.0993$, with Q the volume flow rate and Δp the fan pressure rise (outlet static pressure minus inlet total one). The measurements have been carried out at constant rotational speed Ω of 2,400 rev/min; depending on
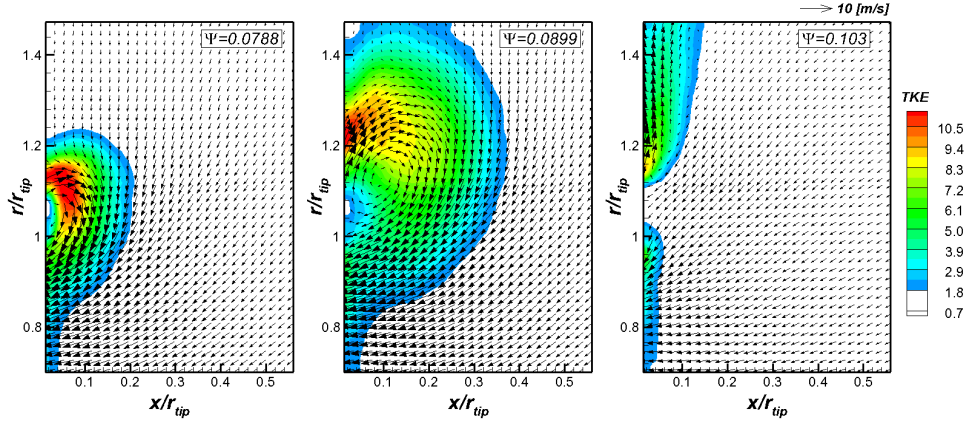
Figure 2: Vectorial representation of time-mean flow field with superimposed the contour plot of the overall TKE $[m^2/s^2]$. The cases $\Psi = 0.0788$, 0.0899 and 0.103 are presented.

the operating point, the chord-based Reynolds number approximately ranges between 31,000 and 41,000 at the hub and between 186,000 and 188,000 at the tip. During the tests, Δp and Ω have been continuously monitored. The rotational speed has been controlled by means of an optical tachometer and a stripe of reflecting tape stuck on one rotor blade, thus generating a one-per-revolution TTL signal. The gap between the rotating ring and the stationary casing is constituted by 5-mm-width axial and radial parts, see Fig. 1c. In order to investigate the effects of pressure rise on the leakage flow dynamics, three Ψ values have been considered out of the 12 ones previously investigated in Canepa et al (2021), i.e. Ψ=0.0788, 0.0899, 0.103. At these operating points, the most interesting behaviors of the leakage flow have been observed.

The flow field has been investigated in the meridional plane close to the tip gap by means of a 2D-PIV system. Namely, in a rectangular area located at $x = 3$ mm from the ring with an extension of $L_x = 123$ mm and $L_r = 171$ mm, i.e., $r/r_{tip} = 0.698-1.468$ and $x/r_{tip} = 0.014-0.581$, see Fig. 1c. Measurements have been carried out using two cameras with a maximum frame rate of 6 Hz. The axial (u) and radial (v) velocity components have been obtained using a spatial cross-correlation function yielding instantaneous vector fields constituted by 83×116 points on a square grid of steps $\Delta x = \Delta r = 1.5$ mm. In the present measurement campaign, 2000 instantaneous vector fields have been collected and the TTL signal generated by the optical tachometer has been employed as reference signal for the rotor-based ensemble average technique. Since the currently adopted PIV system does not allow using the TTL signal to trigger the PIV acquisition, the PIV snapshots have been ordered a posteriori for the computation of the rotor-based phase averaged field. The instantaneous vector fields have been sorted into 90 phase bins per revolution. In order to increase the statistical reliability, the data have been ensemble averaged over a blade pitch, yielding about 10 meridional distributions based on about 198 samples. Other details on the experimental setup and measuring techniques may be found in Canepa et al (2021).

TIME AVERAGED FLOW FIELD

Figure 2 provides the time-mean velocity fields with superimposed the contour plot of the overall turbulent kinetic energy (TKE). For the case $\Psi = 0.0788$, the leakage flow is directly re-ingested by the rotor. This, together with the region of elevated TKE observed at about $1 <$

$r/r_{tip} < 1.15$, makes this operating condition the most critical one in terms of noise production (see Canepa et al 2019a). A completely different scenario characterizes the flow case at $\Psi = 0.103$: the flow leaving the gap moves outwards radially and exits the measuring plane before entering the rotor. Therefore, the leakage flow does not directly interact with the rotor blades since it first mixes with the incoming flow at larger radii. Additionally, lower values of TKE are observed, with the maximum ones occurring for $r/r_{tip} > 1.1$. The most interesting condition is the case $\Psi = 0.0899$. Here, the time-mean radial velocity ($\overline{v}$) is positive for $r/r_{tip} > 1$, thus leading to a larger recirculating region compared to the case $\Psi = 0.0788$. However, the leakage flow enters the rotor before leaving the measuring plane, differently to the case $\Psi = 0.103$. As shown in the following, a marked radial oscillation of the leakage flow is responsible for the enlarged region of high TKE values for $\Psi = 0.0899$ (see also Canepa et al 2021). Otherwise, the conditions $\Psi = 0.0788$ and 0.103 have been found to be significantly more stable in terms of the leakage flow dynamics. Based on the observations reported above, the present work will focus on the analysis of the case $\Psi = 0.0899$ and the associated unsteady behavior of the leakage flow. The aim is to inspect all the possible source of periodic unsteadiness eventually driving the dynamic behavior of the flow leaving the gap, which could not be necessary linked to the rotor rotational speed. To this end, a POD-based phase averaging technique will be employed for the detailed investigation of the coherent motions affecting the leakage flow for the case $\Psi = 0.0899$.

PROPER ORTHOGONAL DECOMPOSITION OF UNSTEADY FLOW
POD mathematical framework

The proper orthogonal decomposition has been proposed first by Lumley (1970) for the analysis of turbulent flows. Given a certain velocity field (i.e. $u(\boldsymbol{x}, t)$), the POD procedure provides spatial modes $\zeta(\boldsymbol{x})$ (resembling the flow structures) and temporal coefficients $\chi(t)$ (retaining the mode dynamics). In the present work, the successive formulation of Sirovich (1987) has been adopted, in which the POD coefficients are directly obtained as the eigenvectors of the temporal cross-correlation matrix C:

$$CX = \Lambda X \tag{1}$$

where $C = U^T U$, U is the snapshot matrix containing the instantaneous realizations of the field, X is the matrix containing the eigenvectors of C, and Λ is a diagonal matrix with the sorted eigenvalues. Once the POD temporal coefficients are computed from eq. (1), the corresponding spatial modes are obtained by projection as

$$Z = UX\Lambda^{-\frac{1}{2}} \tag{2}$$

where Z is the matrix containing the POD modes $\zeta(\boldsymbol{x})$ normalized with their corresponding eigenvalues. POD can be also used to construct reduced order models providing a filtered snapshot matrix U_K retaining the contribution of the first K modes, which are ranked based on their energy content. This is done by inverting eq. 2:

$$U_K = Z\Lambda^{\frac{1}{2}} X^T \tag{3}$$

where the last $N_t - K$ columns of Z are set to zero.

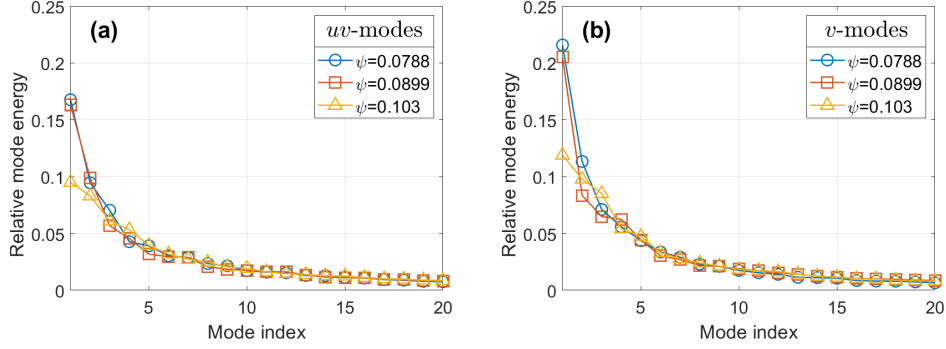Once the POD modes have been computed, a POD-based phase averaging technique has

Figure 3: POD eigenvalues for $\psi = 0.0788$, 0.0889 and 0.103; (a) uv-modes, (b) v-modes.

been implemented, where the reference signal is directly extracted from the leading modes (see Lengani et al 2014). Particularly, if periodic convective structures occur within the flow, coupled modes are typically observed, i.e. modes with similar energy content and spatial distribution (see Legrand et al 2011). Therefore, the corresponding low-order models can be used to sort the instantaneous snapshots based on the main period highlighted by the modes. According to eq. 3, the contribution of the kth POD mode to the ith PIV snapshot can be written as

$$u^{(k)}(x, r, t_i) = \zeta^{(k)}(x, r)\lambda^{(k)\frac{1}{2}}\chi^{(k)}(i) \tag{4}$$

where $\chi^{(k)}(i)$ is the ith element of the kth POD coefficient. Then, if the kth and the $(k+1)^{th}$ modes are coupled and representative of the same convective structures, the phase angle θ_i of the ith record is defined as

$$\theta_i = \frac{\zeta^{(k)}(x_1, r_1)\lambda^{(k)\frac{1}{2}}\chi^{(k)}(i)}{\zeta^{(k+1)}(x_2, r_2)\lambda^{(k+1)\frac{1}{2}}\chi^{(k+1)}(i)} \tag{5}$$

where (x_1, r_1) and (x_2, r_2) are control points used for the computation of each snapshot phase. According to the above mentioned method, all snapshots can be sorted based on their corresponding phase angle and a POD-based phase averaged velocity field can be computed. Since this work aims at the characterization of the radial motions involving the leakage flow, the POD modes of the radial velocity component will be taken as reference for the present POD analysis. This latter has been done considering the quota of the fluctuating velocity field which is not affected by the rotor position. Namely, the periodic components obtained from the rotor-based phase averaging procedure has been removed. This has been done because the rotor-based phase-averaged field, not shown here for brevity, did not show any radial oscillations of the flow leaving the gap, as further discussed by Canepa et al (2021).

POD analysis of rotor unrelated fluctuations

The dominant coherent motions that are not related to the rotor position are studied in this section by means of the Proper Orthogonal Decomposition. Figure 3 depicts the percentage energy of the first 20 POD modes obtained from the POD total kernel (i.e. filling the matrix U with both u and v, uv−modes) and from the radial velocity only (v−modes). For the cases $\Psi = 0.0788$ and 0.0899, the first mode of the total kernel captures more than 16% of the overall energy of fluctuations, while for $\Psi = 0.103$, the leading mode energy is significantly smaller.
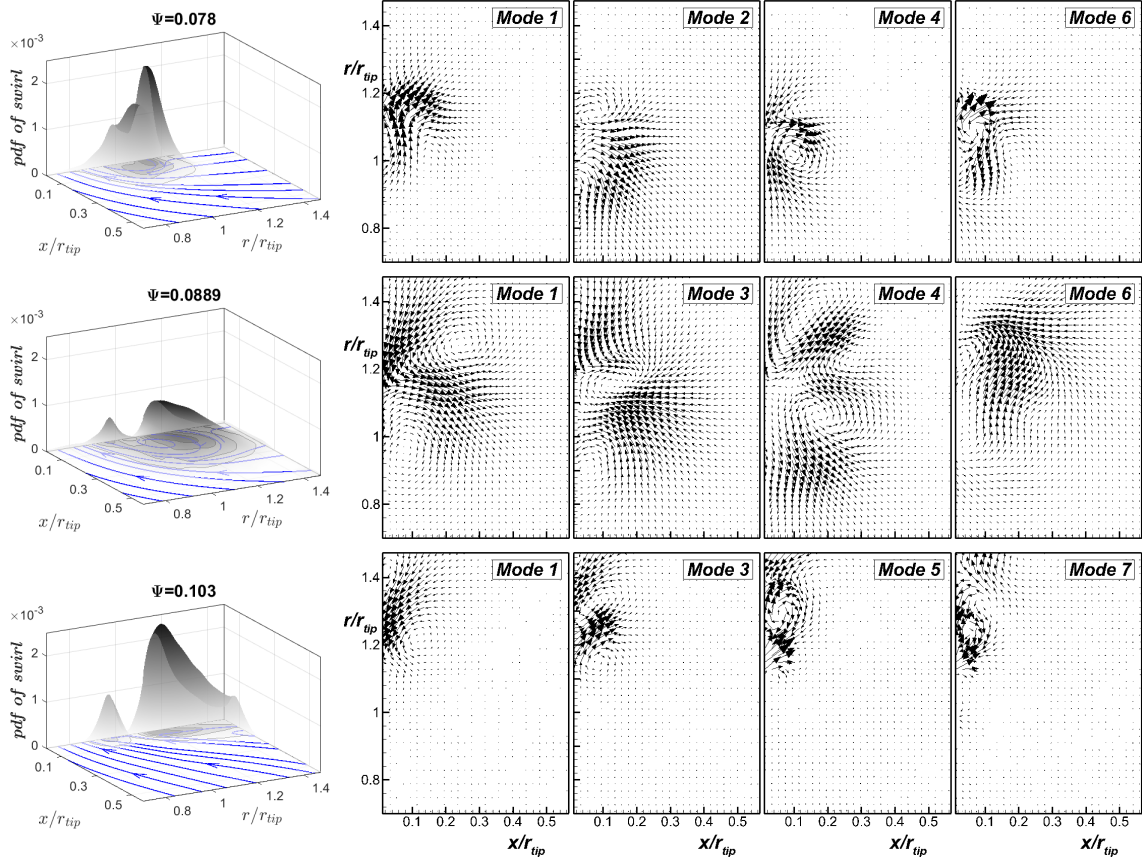
Figure 4: Left plots: *pdf* of vortical events superimposed to the time-mean flow streamlines. *pdf* are computed considering the overall fluctuating velocity field. Right plots: vectorial POD modes of rotor-unrelated fluctuations. The cases $\Psi = 0.0788$, 0.0899 and 0.103 are presented.

This indicates that for the cases $\Psi = 0.0788$ and 0.0899, the rotor-unrelated fluctuations are dominated by few large coherent patterns, which capture a higher quota of the turbulent kinetic energy compared to the case $\Psi = 0.103$. Similar considerations still hold for the POD modes of the radial velocity component. Interestingly, modes 3 and 4 of v show similar energy content for the case $\Psi = 0.0899$, contrary to the other cases. As discussed in the following, these modes are representative of the same coherent structures and they will be referred to for the analysis of the unsteady behavior characterizing the leakage flow for this operating condition.

Figure 4 shows exemplary modes of the total kernel for the three values of Ψ. Modes have been chosen among the first 10 to highlight the main coherent patterns within the fluctuating velocity field reduced by the periodic motions that are phased with the rotor position. Note that the modes, among the first 10, that are similar to those depicted in figure 4 are not reported here for brevity. Moreover, the mode index is not necessarily the same for the cases examined, since the mode rank strictly depends on the analysed flow field. Beside the dominant POD modes, the probability density function (*pdf*) of the occurrence of vortical structures is shown for each case in the form of gray surfaces. Such *pdf* distributions have been obtained by means of a wavelet-based vortex identification technique (see Simoni et al 2016) applied to the overall fluctuating velocity field, i.e. retaining also the rotor-related unsteadiness, differently from what has been done for the computation of the modes. Therefore, the comparison between the *pdf* and the
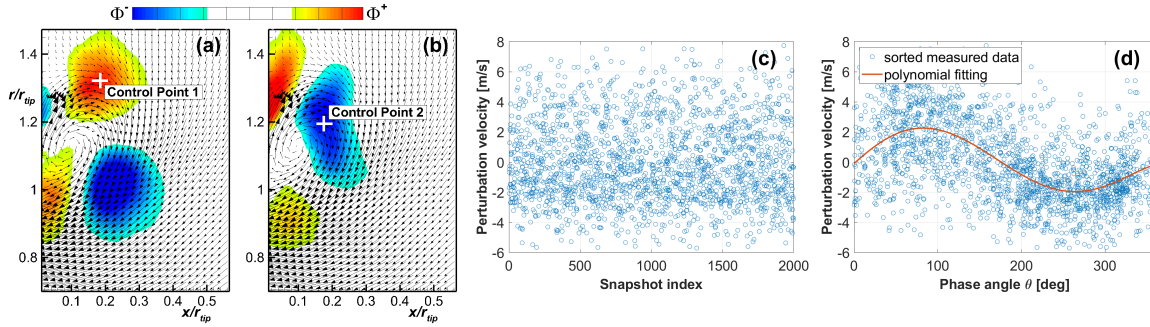
6

Figure 5: Contour plots of normalized modes 3 (a) and 4 (b) of the radial velocity component superimposed to the vectorial representation of the time-mean velocity field; (c) non-sorted perturbation velocity values probed at control point 1; (d) sorted perturbation velocity values probed at control point 1 plotted as a function of the phase angle θ.

POD modes distributions provides information about the spatial location of vortical structures that are or are not related to the rotor position. Particularly, one can clearly see that a dominant *pdf* peak occurs for all cases at the spatial positions where large scale coherent structures are highlighted by the modes. Most of the vortical events observed in the present measuring plane are therefore not phased with the rotor position. For the case $\Psi = 0.0788$, the dominant POD modes resemble vortical structures near the rotor gap and the blade tip. They are representative of the coherent fluctuations of the leakage flow which, for the present case, stays attached to the rotor ring. Differently, the POD modes for the case $\Psi=0.103$ show regions of high vorticity for $r/r_{tip} > 1$, while the energy of the modes is almost null in front of the rotor blades. This clearly indicates that the minor *pdf* peak observed in the blade region (i.e. $r/r_{tip} < 1$) for $\Psi = 0.103$ is substantially linked to rotor related unsteadiness.

The modes computed for the case $\Psi=0.0899$ depict coherent fluctuations covering a wider spatial region than for the other cases; vorticity cores are indeed observed in the blade region as well as above the rotor gap, thus showing similarities with the cases at the lowest and the highest Ψ values. This is consistent with the increment of the *pdf* variance (i.e. the base area). Notice that since the POD modes depicted in Fig. 4 are obtained from the rotor unrelated unsteadiness, the captured flow patterns cannot be ascribed to rotor-related fluctuations. The flow features highlighted by the modes in front of the rotor blade are therefore expected to be linked to a different source of unsteadiness causing the radial motion of the flow leaving the gap. As a consequence, the *pdf* peak observed in the blade region for $\Psi=0.0899$ is due to the superposition of both rotor-related and -unrelated coherent vortical structures. It is mentioned here that based on the inherent three-dimensionality of the instigated flow field, the cores of vorticity observed in the present measuring plane may be the trace of vorticity tubes extending in the circumferential direction, as described in the previous authors' work Canepa et al (2019a). Nevertheless, the radial motions involving the leakage flow for the intermediate value of the pressure rise coefficient will be shown to be well captured by the present set of measurements. Further measurements are being carried out to investigate the evolution of leakage flow fluctuations in the tangential direction.

7

Characterization of the leakage flow dynamics for the case $\Psi = 0.0899$

In order to investigate the oscillating behavior of the leakage flow for the case $\Psi = 0.0899$, the modes of v are further processed in this section. Particularly, modes 3 and 4 have been shown to be coupled in terms of their energy content (see the right plot of Fig. 3, squared symbols) and their spatial distributions, which are reported in Figs. 5a-b, are similar but shifted in the mean flow direction. According to Legrand et al (2011), these modes are therefore representative of the same periodic convective structures and can be used for the computation of a POD-based phase averaged velocity field. This may highlight the existing link between the periodic patterns captured by the modes and the oscillating behavior characterizing the leakage flow for $\Psi = 0.0899$.

According to equation 5, the phase ascribed to each snapshot has been computed based on modes 3 and 4. To do that, two control points have been chosen in regions of opposite sign of the modes (see the white crosses in Fig. 5a-b). Once the correct phase angle has been assigned to each record, the PIV snapshots can be re-ordered and then the corresponding phase averaged field can be computed. Figure 5c reports the rotor-unrelated fluctuations in the radial direction probed at the control point 1. Notice that the PIV snapshots have been acquired with a sampling rate which is significantly smaller than the characteristic frequencies of the flow field, thus the flow records are randomly positioned within the main period highlighted by the modes. Instead, figure 5d reports the sorted velocity values plotted versus the phase angle assigned to the corresponding snapshots. Additionally, the phase averaged values obtained by means of a 5th order polynomial fit to the phase-sorted velocity data is reported with a solid red line, showing a well defined periodic pattern. The present method has been applied to all measuring points to compute a POD-based phase averaged field retaining the periodic coherent motions that are not necessarily related to the rotor rotational speed.

The top plot of Fig. 6 reports the POD-based phase averaged fluctuating velocity field $(\hat{u}, \hat{v})$ at different phase angles, while in the bottom plot the contribution of the time-mean velocity is also included, i.e. $(\hat{u} + \overline{u}, \hat{v} + \overline{v})$. The contour plot of $\hat{v}$ is also superimposed to the corresponding vector fields. It is mentioned here that even if the phase angle of each snapshot is computed with reference to modes 3 and 4 of the radial velocity only, the phase averaged field is computed considering all the dominant modes. The snapshots reported in the top plots of Fig. 6 depict counter rotating vortices that form near the blade tip (see the red and blue circles in the plots). These are the signatures of vorticity tubes which evolve in the tangential direction as described by Canepa et al (2019a). Once formed, they rotate and then move towards the rotor inlet section (see the plots at θ=120° and 300°). For $300° < \theta < 360°$, a new vortex-like structure is expected to occur outside of the measuring plane ($r/r_{tip} > 1.3$), which moves at lower radii leading to the flow pattern observed in the first plot ($\theta = 0°$). It is worth noting that the periodic fluctuations highlighted by the present procedure are characterized by the inversion of the radial velocity component from the largest positive values observed for θ=60°, to the most negative ones occurring for θ=240°. The same trend was not observed in the rotor-based phase-averaged field (see Canepa et al 2019a). Interestingly, when the periodic fluctuations depicted in the top plots of Fig. 6 are added to the time-mean velocity field (bottom plots), this latter exhibits a marked vertical motion in the surrounding of the rotor gap. The large scale vortical structure centered at about r/r_{tip}=1.1 for $\theta = 0°$ stretches in the vertical direction and v again switches from negative to positive values for $r/r_{tip} >1.22$. The present results clearly indicate that the oscillating behavior and the mean flow deformation observed for Ψ=0.0889 are linked to the periodic motion of the coherent structures related to modes 3 and 4 of v, which is
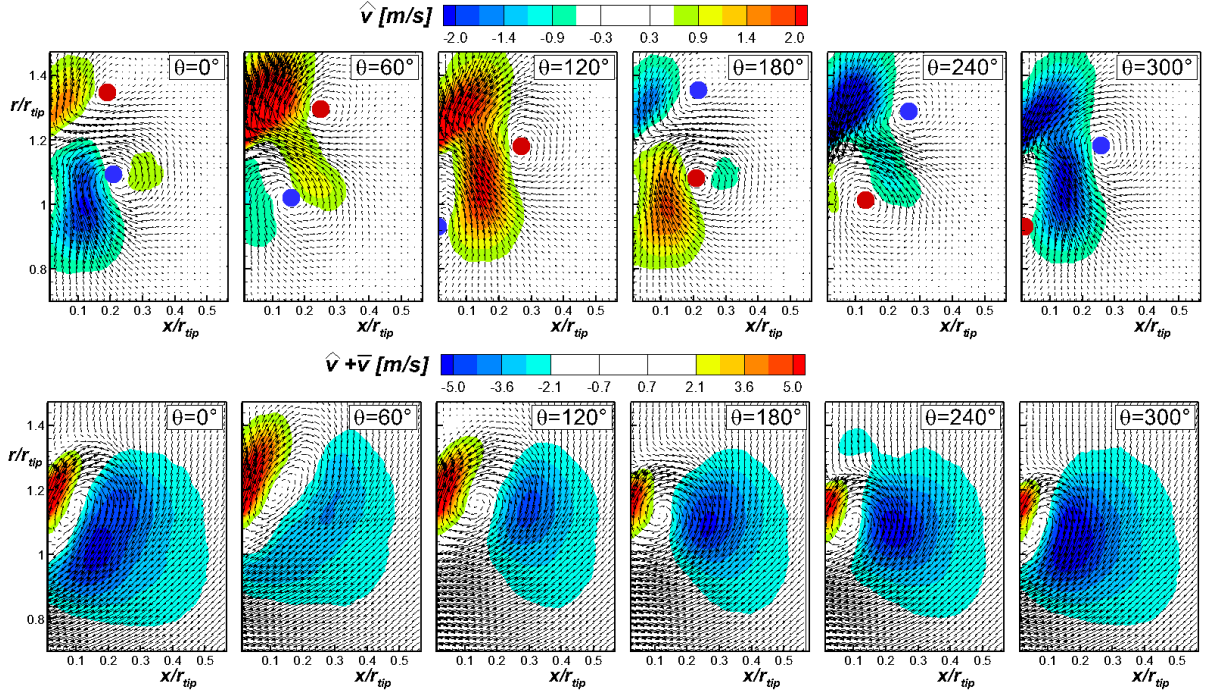
Figure 6: Top: POD-based phase-averaged field of rotor-unrelated unsteadiness at fixed phase angles. Bottom: POD-based phase-averaged field of rotor-unrelated unsteadiness summed up to the time-mean velocity field.

independent of the rotor position. The computation of its own frequency would therefore be of great relevance for the inspection of the associated noise production. Nevertheless, it cannot be directly provided from the present set of measurements due to the low sampling rate adopted. A rough estimation of its value has been instead obtained from the spatial distributions of modes 3 and 4 (Fig. 5). More precisely, the estimated frequency has been computed as the ratio between the time-mean velocity (averaged along the trajectory depicted by the modes) and the distance, in the mean flow direction, between two points of the same mode sign. The so derived value has been found to be about 30 Hz. The assumption behind the present approach is that the observed phenomenon is purely convective, which is not necessarily the case for the present flow configuration. Further investigation will be therefore carried out in a future work for the detailed inspection of the frequency content of the flow patterns observed in Fig. 6.

Phase averaged distributions of turbulent kinetic energy and its production.

This section reports the phase-averaged TKE distributions based on the blade period and the periodic motion extracted by the modes. Additionally, the TKE production has been computed based on phase averaged quantities (see e.g., Michelassi and Wissink 2015):

$$\langle P_{TKE} \rangle = \left\langle \overline{u^2} \right\rangle \frac{\partial \langle U \rangle}{\partial x} + \left\langle \overline{v^2} \right\rangle \frac{\partial \langle V \rangle}{\partial r} + \langle \overline{uv} \rangle \left(\frac{\partial \langle U \rangle}{\partial r} + \frac{\partial \langle V \rangle}{\partial x} \right) \tag{6}$$

here $\langle \cdot \rangle$ denotes phase dependent quantities, (u, v) is the turbulent velocity field, and (U, V) is the phase averaged one. The stress terms appearing in eq. (6) have been computed from the
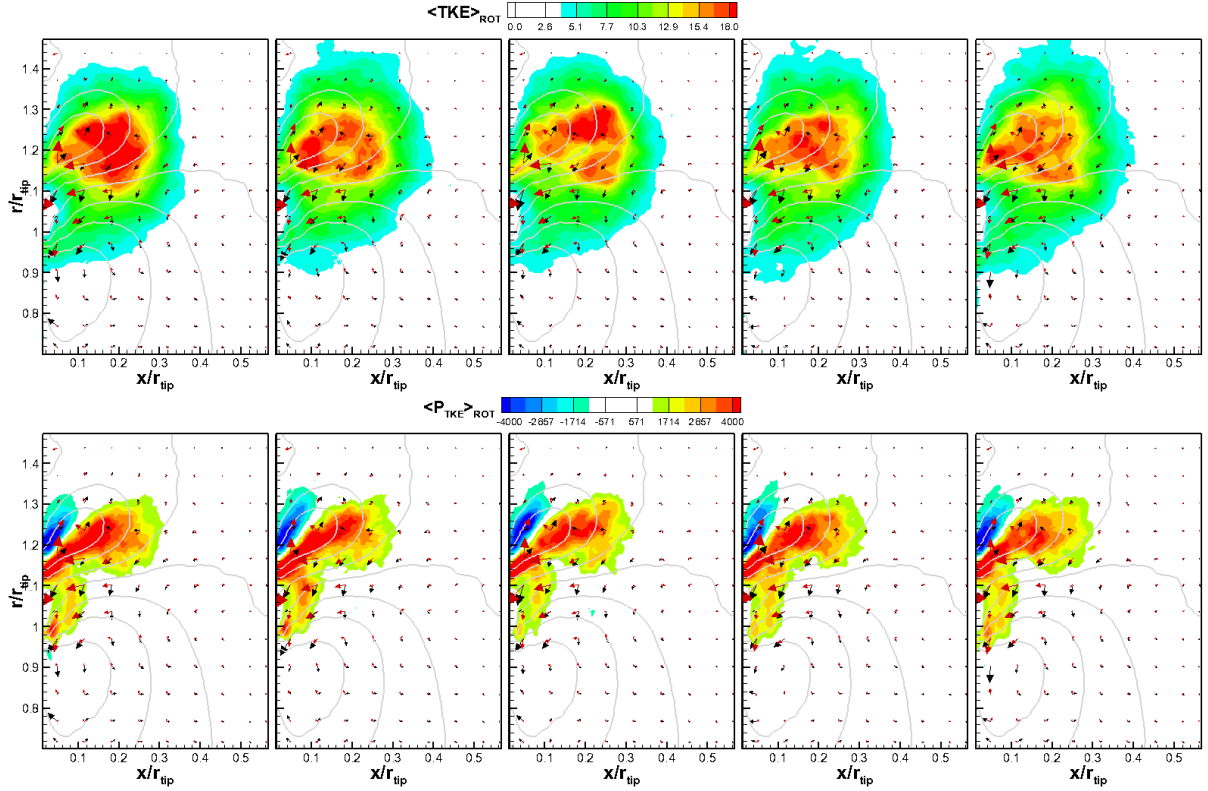
9

Figure 7: Top: contour plot of rotor-based phase-averaged turbulent kinetic energy based on blade period $\langle TKE \rangle_{ROT} \, [m^2/s^2]$. Plots are shown at the phase angles $\theta = 0°, 72°, 144°, 216°$ and $288°$. Bottom: Contour plot of phase-averaged turbulent kinetic energy production based on blade period $\langle P_{TKE} \rangle_{ROT} \, [m^2/s^3]$. Black and red vectors represent the axial and radial velocity gradients, respectively, of the phase averaged field. Contour lines of time-mean axial velocity are shown with grey color.

non-periodic unsteadiness, which has been obtained by subtracting the rotor- and POD-based phase averaged fields from the overall fluctuating velocity. Then, the measured data have been sorted based on the corresponding phase index of the two periodic patterns and then combined with the strain tensor accounting for the deformation of the mean and phase dependent fields.

Figure 7 shows the contour plots of the rotor-based phase-averaged turbulent kinetic energy $\langle TKE \rangle_{ROT}$ and its related production $\langle P_{TKE} \rangle_{ROT}$. Plots are shown at the phase angles $\theta = 0°, 72°, 144°, 216°$ and $288°$. Additionally, the gradient vectors of U and V are depicted with black and red color, respectively, to highlight the regions of high strain. Interestingly, both $\langle TKE \rangle_{ROT}$ and $\langle P_{TKE} \rangle_{ROT}$ show negligible variations with the phase angle, thus the turbulent kinetic energy and its production do not depend on the rotor phase. Moreover, the maximum of both these quantities is observed in the gap region where the largest gradients of the phase-averaged field occur. Turbulence production is therefore given by the combination of high levels of phase dependent strain with turbulent stresses. It is worth noting that both positive and negative values of $\langle P_{TKE} \rangle_{ROT}$ are observed for all phase angles. The occurrence of negative $\langle P_{TKE} \rangle_{ROT}$ indicates energy back transfer from the unresolved unsteady field to the corresponding phase-averaged one. However, the integral value of $\langle P_{TKE} \rangle_{ROT}$ is positive, thus leading to the increment of the overall turbulence level within the flow field.
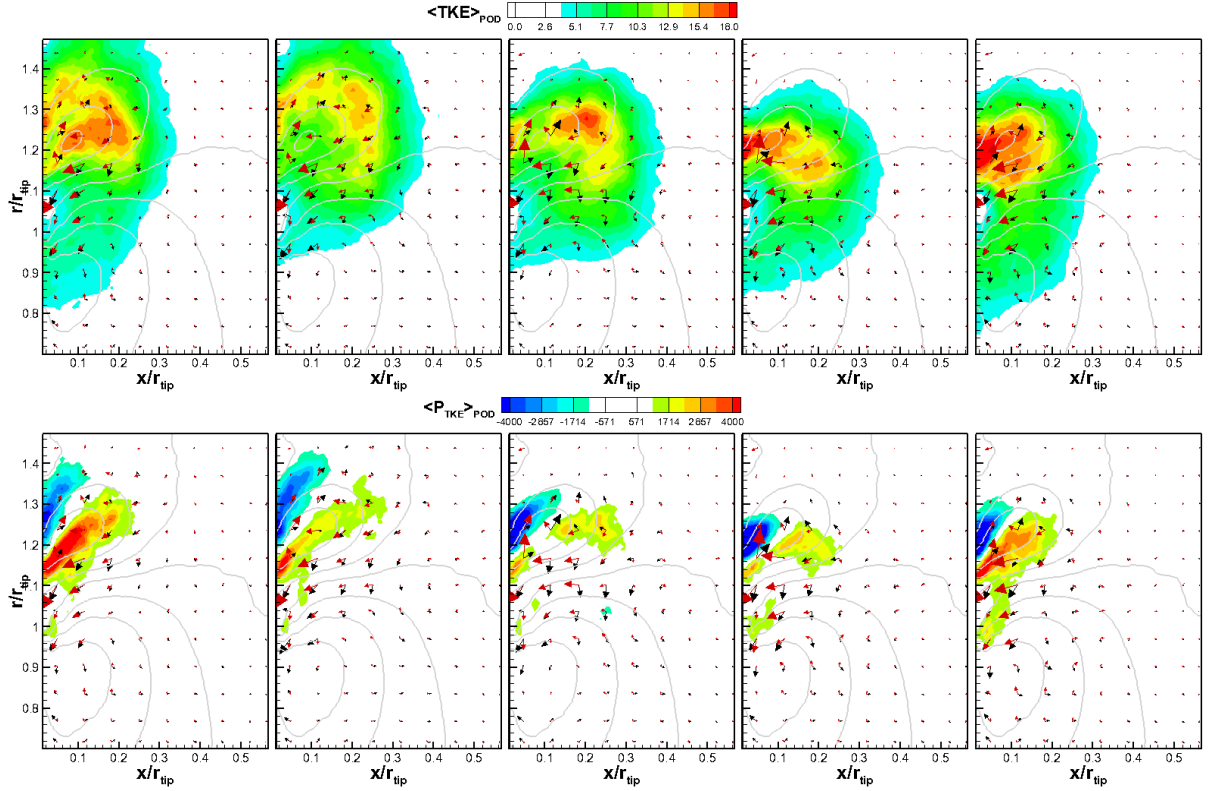
Figure 8: Top: contour plot of POD-based phase-averaged turbulent kinetic energy $\langle TKE \rangle_{POD} \, [m^2/s^2]$. Bottom: Contour plot of POD-based phase-averaged turbulent kinetic energy production $\langle P_{TKE} \rangle_{POD} \, [m^2/s^3]$. Plots are shown at the phase angles $\theta = 0°, 72°, 144°, 216°$ and $288°$. Black and red vectors represent the axial and radial velocity gradients, respectively, of the phase averaged field. Contour lines of time-mean axial velocity are shown with grey color.

A completely different scenario characterizes the POD-based phase averaged TKE and related production, see Fig. 8. The $\langle TKE \rangle_{POD}$ distribution shows high dependence on the phase angle in terms of its maximum values and their spatial positions. The highest values of $\langle TKE \rangle_{POD}$ always occur for $r/r_{tip} > 1$, while lower ones are observed in front of the blade. Additionally, the region of maximum TKE moves at different radii within the reference period. This behavior well resembles the one observed in the phase-averaged field reported in Fig. 6. This indicates that the periodic pattern highlighted by the POD analysis may cause turbulence transport at different radial locations. Since the interaction between the flow unsteadiness generated by the leakage flow and the rotating fan may produce different level of acoustic noise depending on the region where interaction occurs, the turbulence transport here highlighted should be considered for the acoustic optimization of the aerodynamic component here tested. Interestingly, negative values of $\langle P_{TKE} \rangle_{POD}$ dominate, thus the periodic motion captured by the POD modes is mostly responsible for energy back transfer from the unresolved to the POD-based phased-averaged velocity field. This behavior is different to what observed instead from the rotor-based phase averaging method.

CONCLUSIONS

The present work presented a POD based analysis of the unsteady leakage flow of an axial fan equipped with rotating shroud. Three values of the loading coefficients have been examined, among which the case $\Psi = 0.0899$ showed a strongly unsteady behavior of the flow leaving the gap. For this operating condition, the leakage flow was found to move at different radial positions, while it was significantly more stable for the other cases. The POD based technique here adopted clearly showed that this behavior is governed by the occurrence of coherent vortical structures characterized by a marked periodicity that is different from the blade passing period. Indeed, the rotor-based phased-averaged field reported in the previous authors' work Canepa et al (2021) did not show any coherent motions affecting the leakage. Herein, POD-based phase-averaged TKE and P_{TKE} distributions have been computed and then compared to those obtained based on the rotor reference. Rotor-unrelated fluctuations have been shown to provoke high turbulence transport at different radial positions, thus possibly affecting the noise production of the rotor. The phase averaging procedure here adopted is therefore thought to be functional to the acoustic noise and vibration optimization of a wide range of aerodynamic components, other than that tested here.

References

Canepa E, Cattanei A, Zecchin FM, et al (2016) An experimental investigation on the tip leakage noise in axial-flow fans with rotating shroud. Journal of Sound and Vibration 375:115–131

Canepa E, Cattanei A, Jafelice F, et al (2018) Effect of rotor deformation and blade loading on the leakage noise in low-speed axial fans. Journal of Sound and Vibration 433:99–123

Canepa E, Cattanei A, Mazzocut Zecchin F (2019a) Leakage noise and related flow pattern in a low-speed axial fan with rotating shroud. International Journal of Turbomachinery, Propulsion and Power 4(3):17

Canepa E, Cattanei A, Zecchin FM, et al (2019b) Large-scale unsteady flow structures in the leakage flow of a low-speed axial fan with rotating shroud. Experimental Thermal and Fluid Science 102:1–19

Canepa E, Cattanei A, Moradi M, et al (2021) Experimental study of the leakage flow in an axial-flow fan at variable loading. International Journal of Turbomachinery, Propulsion and Power 6(4):40

Fukano T, Jang CM (2004) Tip clearance noise of axial flow fans operating at design and off-design condition. Journal of sound and vibration 275(3-5):1027–1050

Fukano T, Takamatsu Y, Kodama Y (1986) The effects of tip clearance on the noise of low pressure axial and mixed flow fans. Journal of sound and vibration 105(2):291–308

Legrand M, Nogueira J, Lecuona A (2011) Flow temporal reconstruction from non-time-resolved data part I: mathematic fundamentals. Exp Fluids 51(4):1047–1055

Lengani D, Simoni D, Ubaldi M, et al (2014) POD analysis of the unsteady behavior of a laminar separation bubble. Experimental Thermal and Fluid Science 58:70–79

Longhouse R (1978) Control of tip-vortex noise of axial flow fans by rotating shrouds. Journal of sound and vibration 58(2):201–214

Lumley JL (1970) Stochastic tools in turbulence. Applied Mathematics and Mechanics, vol 12

Magne S, Moreau S, Berry A (2015) Subharmonic tonal noise from backflow vortices radiated by a low-speed ring fan in uniform inlet flow. The Journal of the Acoustical Society of America 137(1):228–237

Michelassi V, Wissink JG (2015) Turbulent kinetic energy production in the vane of a low-pressure linear turbine cascade with incoming wakes. International Journal of Rotating Machinery 2015

Moreau S, Sanjose M (2016) Sub-harmonic broadband humps and tip noise in low-speed ring fans. The Journal of the Acoustical Society of America 139(1):118–127

Na GD, Kameier F, Springer N, et al (2017) Urans simulations and experimental investigations on unsteady aerodynamic effects in the blade tip region of a shrouded fan configuration. In: Turbo Expo: Power for Land, Sea, and Air, American Society of Mechanical Engineers, p V001T09A003

Piellard M, Coutty BB, Le Goff V, et al (2014) Direct aeroacoustics simulation of automotive engine cooling fan system: effect of upstream geometry on broadband noise. In: 20th AIAA/CEAS Aeroacoustics Conference, p 2455

Simoni D, Lengani D, Guida R (2016) A wavelet-based intermittency detection technique from PIV investigations in transitional boundary layers. Exp Fluids 57(9):145

Sirovich L (1987) Turbulence and the dynamics of coherent structures. part I-III. Q Appl Math 45:561–590

Zenger FJ, Renz A, Becher M, et al (2016) Experimental investigation of the noise emission of axial fans under distorted inflow conditions. Journal of Sound and Vibration 383:124–145

Zhu T, Lallier-Daniels D, Sanjosé M, et al (2018) Rotating coherent flow structures as a source for narrowband tip clearance noise from axial fans. Journal of Sound and Vibration 417:198–215